ADVANCED FUNCTIONAL MATERIALS
www.afm-journal.de

Electrochemical Reactivity and Stability of the Fe Electrode in Alkaline Electrolyte

*Shu Fen Tan, Hanglong Wu, Joseph S. Manser, Duhan Zhang, Maria Ronchi, Sylvia Smullin, Yet-Ming Chiang, and Frances M. Ross**

Fe anodes are emerging as cost-effective components in long duration storage applications, with a benefit being the high natural abundance of Fe. Additive and electrode design have advanced the performance of Fe electrodes, but a more precise understanding of the electrode formation process and failure mechanisms is important for continued optimization. These interfacial electrochemical processes, which involve short-lived intermediate species, require analysis with high spatial and temporal resolution to provide a full picture. This study therefore explores the behavior of the Fe electrode in alkaline electrolyte using electrochemical liquid cell transmission electron microscopy, extending the technique toward high pH (10–13) conditions. By combining identical location imaging and diffraction, in situ imaging, and benchtop experiments, this study shows distinct microstructural changes on cycling as a function of pH, in particular the appearance of multiple electrodeposited Fe species and a passivation layer. The dependence on electrochemical parameters is discussed, showing that the observations can be related to stability predictions from the Pourbaix diagram. However, it is also necessary to consider kinetic effects, such as the solubility and diffusion of soluble species. Strategies to control these material transformations are discussed as a function of potential, along with opportunities for further optimizing the Fe electrode.

1. Introduction

Fossil fuels are environmentally unfriendly but account for a large fraction of the world's total energy supply, 82% in 2022.[1] Reducing pollution and greenhouse gas emission is driving a shift to sustainable renewable sources for electricity generation in order to transition to a net-zero emissions energy system. Since solar and wind are intermittent sources dependent on weather conditions and seasonal and diurnal variations,[2] energy storage systems are needed that are low-cost, safe, scalable and geographically independent.

Batteries are key technologies to meet these requirements for grid-scale storage. The best established of these are lithium-ion batteries (LIBs), vanadium redox flow batteries, lead-acid batteries, and metal-air batteries. Case studies suggest that electrochemical energy storage for long duration grid-scale applications requires system costs below \$50/kWh.[3] For LIBs, the high capital cost and environmental impact hinder their use for long-duration storage that requires infrequent cycling. Vanadium redox flow batteries also suffer from high capital costs and fluctuating vanadium prices, in spite of the good scalability of the modular cell architecture.[4] Additional concerns for aqueous metal-air batteries include increased anode costs and reversibility issues at the anode.[5]

These considerations make metals such as Fe, Zn, Na, and Al interesting candidates for electrodes owing to their low cost and high natural abundance. Fe was first examined early in the development of batteries[6] and Fe-based materials are being explored for next-generation electrodes in energy storage and conversion applications, including both batteries[5,7] and fuel cells.[8] Fe-air and Zn-Fe grid applications have been developed in Europe and South America.[7d,9] Fe is particularly low cost, with iron ore at ≈\$0.12/kg, and is abundant across all continents. Fe therefore has one of the lowest theoretical costs-per-stored-charge, ≈\$0.13/kAh, among redox active species, given that the theoretical specific capacity of Fe(III) → Fe(0) is 1440 mAh g^{-1}.[10] Furthermore, a significant advantage over the next lowest cost metal, Zn, is the reduced formation of dendrites during cycling in alkaline electrolytes, and avoidance of the consequent failure mechanism.[5,7d]

S. F. Tan, H. Wu, D. Zhang, Y.-M. Chiang, F. M. Ross
Department of Materials Science and Engineering
Massachusetts Institute of Technology
Cambridge, MA 02139, USA
E-mail: fmross@mit.edu

S. F. Tan
School of Materials Science and Engineering
Nanyang Technological University
Singapore 639798, Singapore

J. S. Manser, M. Ronchi, S. Smullin, Y.-M. Chiang
Form Energy, Inc.
Somerville, MA 02143, USA

S. Smullin
VEIR, Inc
Woburn, MA 01801, USA

The ORCID identification number(s) for the author(s) of this article can be found under https://doi.org/10.1002/adfm.202407561

DOI: 10.1002/adfm.202407561

According to its Pourbaix diagram,[6,11] Fe exists in multiple phases depending on the potential and pH of the electrolyte. Fe electrode battery designs generally involve highly alkaline electrolytes (up to pH = 15) due to their compatibility with desirable redox couples at the positive electrode and the lack of dendritic growth, mentioned above, in alkaline environments. In the alkaline regime, the most important species present during cycling are passivation species such as iron hydroxide and soluble species such as ferrite ions, both of which may participate in charge and discharge, depending on the electrolyte pH. However, a critical issue is the stability and morphological evolution of the Fe electrode during cycling in strong alkaline (as well as in strong acidic) media. Improvements have been made in additive[12] and electrode[13] design to optimize performance, yet challenges of Fe electrodes such as dissolution, passivation and self-discharge in the high pH range must be understood more deeply for continued development.

A regime in which morphological changes are especially important is in the first few charge–discharge cycles. To achieve a stable discharge capacity[14] and allow for immediate use in-product, a formation process of the Fe electrode is typically required during manufacturing. This involves carrying out tens of charge-discharge cycles to improve the wetting of the iron electrode, reduce the impurities and more importantly, increase the accessible electrochemically active surface area (EASA).[13,14b] Electrochemical measurements show reaction phenomena taking place during the formation process,[14b] and a study of the topographic evolution of the Fe electrode during potential cycling at pH 13.7 shows that sequential oxidation and reduction reactions do indeed lead to morphological changes.[15] One such change is the development of a passivating iron hydroxide/oxide layer during discharge that may reduce the EASA over the course of the cycling, until the electrolyte is no longer in contact with metallic iron. This iron hydroxide/oxide layer prevents complete oxidation and limits the full utilization of the iron electrode capacity.[16] A detailed understanding of electrode performance therefore requires experimental verification of the location and nature of the species present, both passivating and soluble, their relationship to expectations from the Pourbaix diagram, and the effect of the formation process on the reversibility and utilization of the Fe electrode.

The technique of electrochemical liquid cell TEM[17] has been shown to enable imaging of morphological changes at electrodes with the high spatial and temporal resolution required for probing reaction mechanisms. Here, we use this technique to correlate structural and electrochemical changes at the Fe electrode in aqueous alkaline electrolytes. This requires extending the operating pH range of electrochemical liquid cell TEM toward the higher values that are of most relevance to battery operation. Here, we focus on the pH range 10–13. This pH range holds significant interest in the Fe Pourbaix diagram as it marks a transition of the primary soluble species from Fe^{2+} to $HFeO_2^-$ ions while the final stable solid products remain unchanged. This range also covers the conditions under which the Fe electrode transitions from a passivation to a corrosion regime, with the boundary between these two regimes occurring at around pH = 12.5.[11] The experiments show that liquid cell TEM is useful in characterizing battery reactions under aggressive chemical conditions, opening opportunities to uncover fundamental mechanisms that may lead to strategies for optimizing electrodes in practical materials systems. We anticipate that the combination of electrochemical kinetic liquid cell TEM data with equilibrium thermodynamic insights from the Pourbaix diagram will deepen our understanding of the underlying mechanisms governing metal anode performance in the Fe and other electrochemical systems.

2. Results

In the following sections we start by describing microstructural changes at the Fe electrode as probed using cyclic voltammetry (CV) (**Figures 1–4**). In particular, we will consider the evidence for soluble Fe species upon potential cycling and a passivated oxide layer upon switching from reducing to oxidizing potentials. We then discuss calibration and interpretation of these results in terms of the solubility of the products and consider the implications for understanding the processes taking place during battery operation. Since liquid cell TEM has predominantly been used in neutral or acidic conditions, we also assess the stability of the Fe electrode in alkaline electrolyte under electron beam irradiation with no bias. By combining benchtop experiments with different modes of liquid cell TEM (identical-location imaging and diffraction, which measure the same electrode area before and after cycling, and in situ imaging, which measures during cycling), we demonstrate that the presence and reactions of various soluble and insoluble phases on the Fe electrode during potential cycling can be interpreted through stability predictions from the Pourbaix diagram (**Figure 5**). However, we also emphasize the importance of considering kinetic effects, including the solubility and diffusion of soluble species, electrolyte depletion and the kinetics of discharge product formation and accumulation.

2.1. Electrochemical Response of the Fe Electrode in Alkaline Electrolyte

Our electrochemical cycling experiments are described in Figure 1 with additional details in the Experimental section. We used electrochemical liquid cell chips incorporating three electrodes fabricated by lift-off patterning of a Pt layer 20 nm in thickness. On these chips, as-received, only the Pt on the SiN_x viewing window is electrochemically active, with each electrode having several hundred μm^2 area, and the remaining metal track is covered by an insulating layer. We used electron beam deposition through a shadow mask to pattern a thin Fe film (thickness 35–60 nm, area 2×10^6 μm^2) over the original Pt working electrode as illustrated in the schematic (Figure 1a) and optical image (Figure 1b). Approximately 300 μm × 30 μm of the Fe area is visible in the window region of the chip. TEM imaging (Figure 1c) and diffraction (Figure 1d) show that the as-deposited Fe is polycrystalline with 5–10 nm average grain size and the expected body centered cubic structure.

We first measure the electrochemical signal arising from reactions at the Fe thin film. Figure 1 shows a typical sequence of CV cycles (Figure 1e; full data set in Figure S4, Supporting

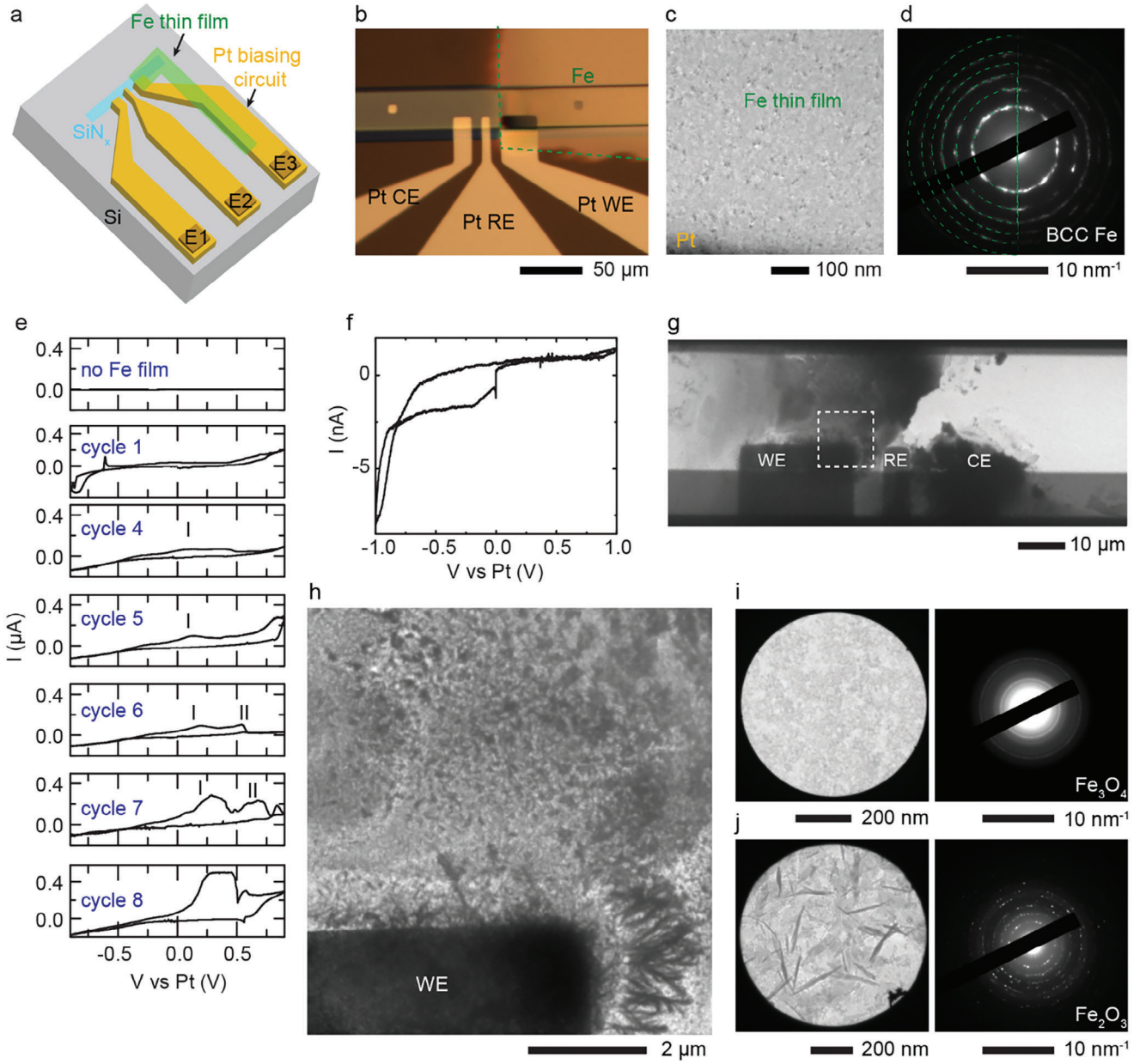

Figure 1. Potential cycling of Fe electrode in alkaline electrolyte at pH = 10. a,b) Schematic and light microscopy images of a commercially available biasing chip with 20-nm thick Pt electrodes (yellow) crossing the viewing window (cyan) and connected to three contact pads E1, E2 and E3 to act as counter, reference and working electrodes respectively. A thin Fe deposited film is shown as the L-shaped green polygon. c,d) TEM image (c) showing the as-deposited Fe thin film with selected area electron diffraction (SAED) pattern (d) confirming the BCC Fe structure. e) Selected cyclic voltammograms recorded on the benchtop, scanning from 0 V to −0.9 V to +0.9 V at 10 mV s^{-1} in 0.1 mM KOH electrolyte in the electrochemical liquid cell with electrodes as-received and Fe thin film added as shown in (a). The full series is shown in Figure S4 (Supporting Information). f) Expanded view of the first panel of (e) to show the lower current without Fe. g) Overview TEM image showing newly-deposited Fe species over the working electrode (WE), reference electrode (RE), and counter electrode (CE) after potential cycling on the benchtop. See Figure S5 (Supporting Information) for an image pair of pristine Fe electrode before and after cycling. h) Enlarged TEM image showing newly deposited needle-like Fe species: i) TEM images and corresponding SAED of Fe_3O_4 and j) Fe_2O_3 at WE after twenty CV cycles.

Information) and post-cycling TEM results obtained using a Pt quasi-reference electrode. These initial experiments were carried out using an electrolyte of pH = 10 (0.1 mM KOH) to explore the $Fe(OH)_2$ stability regime where we expect to see passivation products, as discussed below; this pH also reduces the risk of etching the Si components of the liquid cell. Higher pH values, as needed to explore the regime of soluble products, will be described later. We used a protocol whereby the cell is cycled in the reduction direction from 0 to −0.9 V, which is expected to largely reduce the surface native oxide layer on the Fe anode, and then is scanned in the oxidation direction from −0.9 to +0.9 V, all at a scan rate of 10 mV s^{-1}. The voltage is subsequently returned to

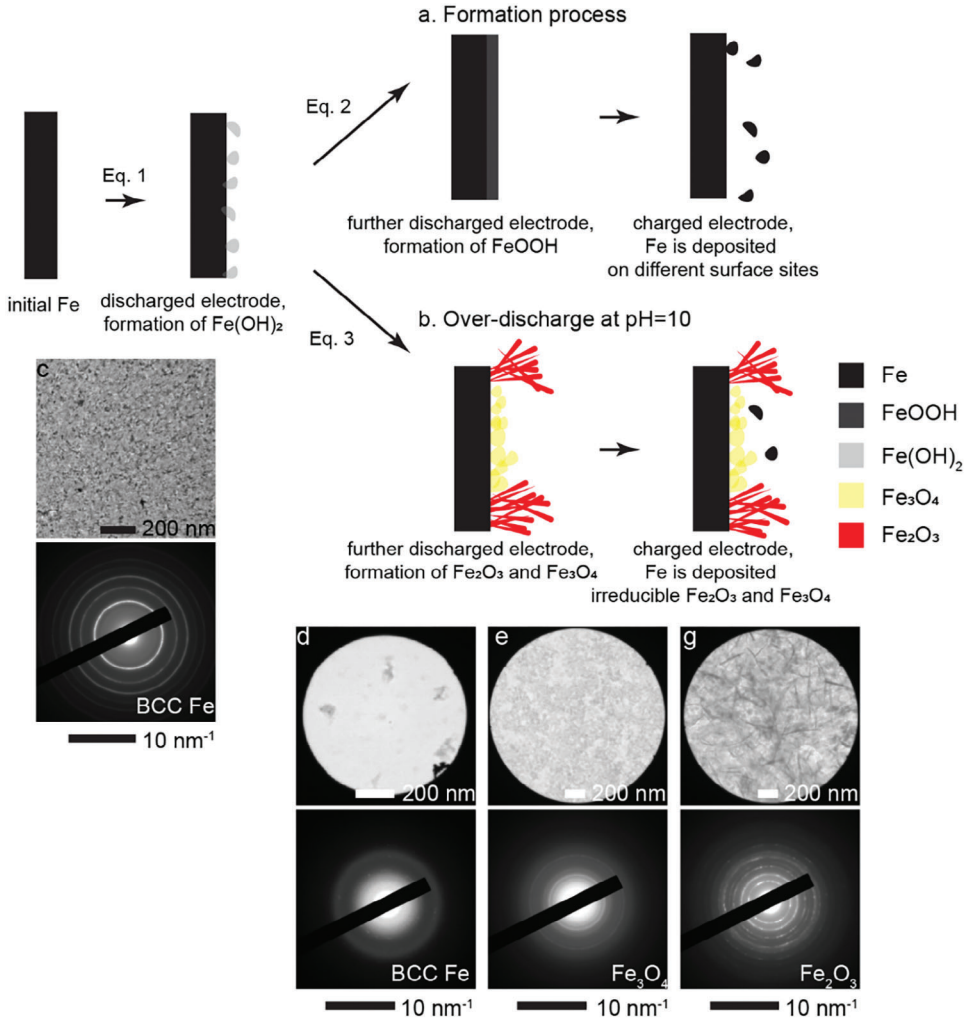

Figure 2. Electrochemical processes during formation of the Fe electrode. a) Schematic of formation process of complete reduction of passivated Fe hydroxide film. Adapted from Manohar et al.[16] with permission under a Creative Commons CC-BY License. Copyright 2012 IOP Publishing. b) Further oxidation to deeply discharged Fe products at pH = 10. c) TEM image showing the initial BCC Fe thin film with its corresponding diffraction pattern. d) TEM images and corresponding SAED showing the electrodeposited BCC Fe, e) Fe_3O_4 and f) Fe_2O_3 found after 20 cycles of potential cycling at pH = 10.

zero and the cycle is repeated up to 20 times. Initially the electron beam remains off until the end of the cycling or at certain points between cycles to avoid beam effects, which we consider below.

The CV in Figure 1e shows a distinctive signature of the presence of the Fe layer: oxidation peaks (peak I and II) observed at +0.2 to 0.3 V and at +0.5 V (precise positions varying with cycle number) with respect to the Pt quasi-reference electrode. These peaks are not present for control experiments without Fe (Figure 1f). We therefore attribute these peaks to the formation of Fe species during cycling. However, these peaks undergo progressive changes over the first several cycles that complicate identification. We note that currents are in the 10^{-7} A range for the chips with Fe (giving current density ≈ 0.1 A/m^2), while in chips without Fe (and therefore smaller electrode areas) the current is below ≈10^{-9} A in the same electrolyte and cycling conditions.

2.2. Reference Electrode Calibration Within the Liquid Cell

In electrochemical experiments involving a quasi-RE, calibration of the RE potential is essential to ensure accurate electrochemical interpretation. RE potential calibration can be conducted by either comparing the quasi-RE against a standard RE, such as Ag/AgCl, which has a well-established potential, or by using a reversible redox species with known redox potentials in the electrolyte as an internal reference.[18] For electrochemical liquid cell experiments, the most promising and effective approach for RE potential calibration has been reported to involve incorporating a standard RE on the tip of the in situ TEM holder.[18b] Therefore, in this study, we employ this method by comparing the on-chip Pt quasi-RE at pH = 10 against a standard Ag/AgCl saturated RE positioned within the liquid cell holder and near the tip (see Experimental Section). By matching the positions of Pt redox peaks we roughly determine the experimental voltage

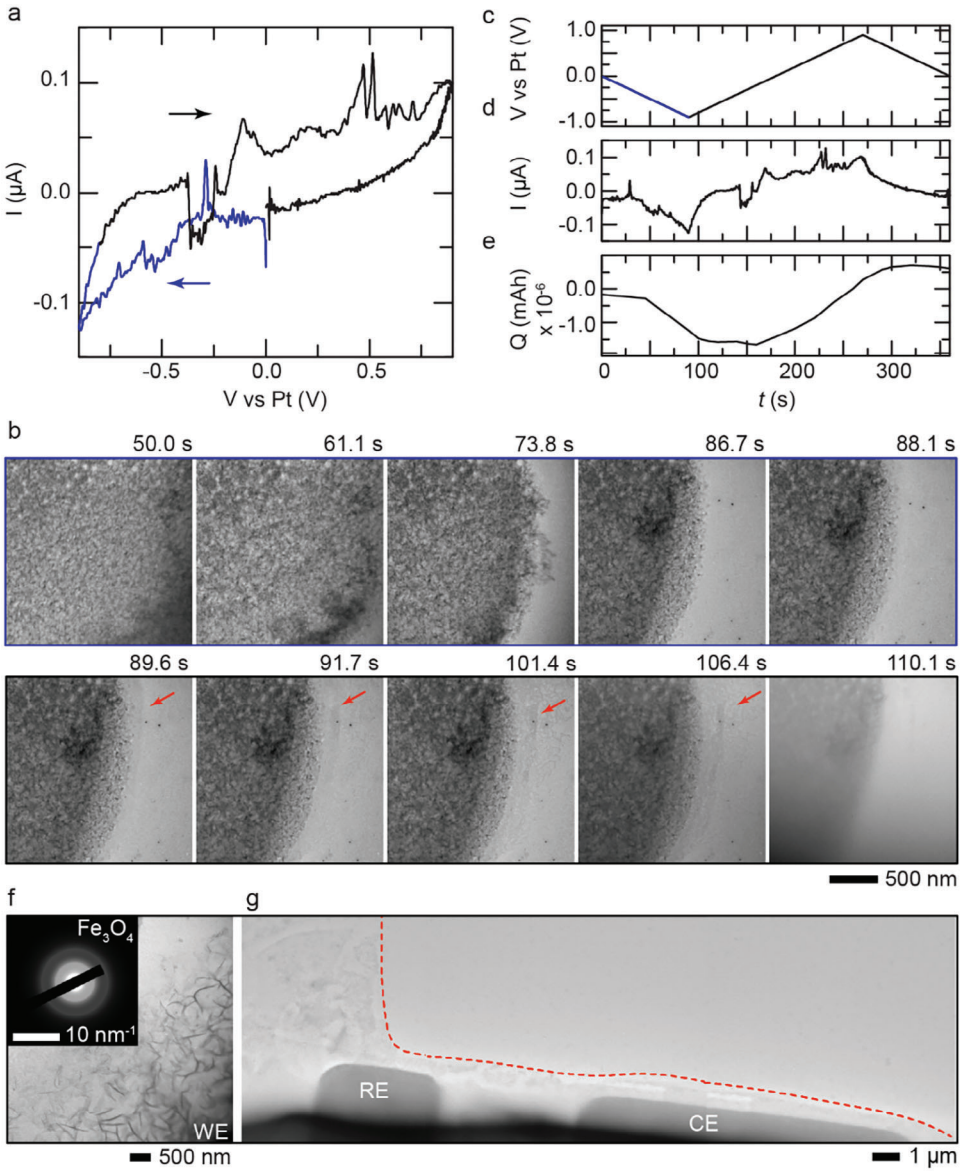

Figure 3. In situ cyclic voltammetry (CV) measurements of Fe electrode at pH = 10 in 0.1 mM KOH electrolyte. (a) Selected CV cycle scanning from 0 V to −0.9 V to +0.9 V at 10 mV s^{-1} using the electrochemical liquid cell with electrode geometry shown in Figure 1a. All CVs can be found in Figure S7a (Supporting Information). b) Images from a TEM video (Video S1, Supporting Information) obtained with an electron flux of 19 e^{-} $Å^{-2}$ $2\ s^{-1}$. The potential for each image is indicated by outlines with reduction in blue and oxidation in black. Red arrows indicate the formation of a thin layer upon switching from reduction to oxidation. c,d) Potential and current response as a function of time during CV shown in (a). e) Accumulated charge versus time, extracted by integrating the current during the CV cycle. f) TEM image showing newly-deposited Fe species at WE, RE and CE: Fe_3O_4 at WE (insets showing the diffraction pattern) after CV cycle shown in (a). g) Overview TEM image showing the newly-deposited Fe species after potential cycling at WE, RE, and CE. Dotted red lines in (f) and (g) show a blocking layer formed across the electrodes.

offset (Figure S1, Supporting Information). Our results suggest that a measurement of 0 V_{Pt} is equivalent to −0.8 $V_{Ag/AgCl}$ and −0.6 V_{SHE}. In other words, potential sweeping between −0.9 to +0.9 V_{Pt} is equivalent to a sweep from −1.5 to +0.3 V_{SHE}. This calibration, even though approximate, helps us attempt to match measured peaks in CV and images of etching or passivation with expectations based on the literature and Pourbaix diagram.[11a]

Experimental considerations in such matching include the possibility of drift in the quasi-RE and the depletion of species in the limited electrolyte volume; we also note the importance of avoiding extraneous electrochemical reactions and voltage drops given the weak signals and small electrode areas present in the electrochemical liquid cell. As an example, in measurements of chips with Cu instead of Pt electrode contacts, we found the results are compromised by galvanic corrosion at the Fe/Cu junction (Figure S2, Supporting Information). We do not observe this phenomenon for Pt chips, at least over the time scale of the typical liquid cell experiment (Figure S3, Supporting Information). In spite of these challenges, the general repeatability of the electrochemical and image data over multiple separate experiments

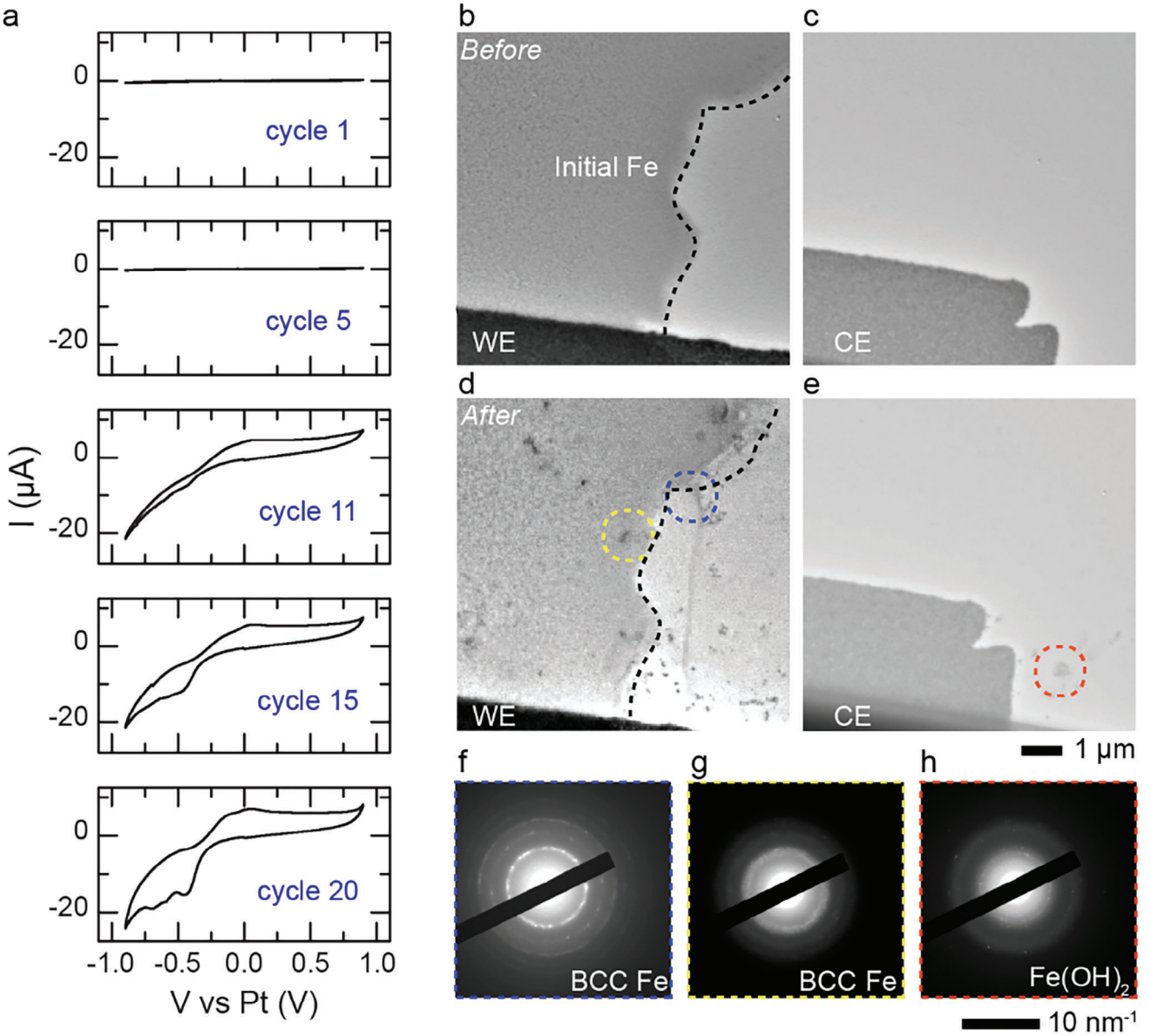

Figure 4. Potential cycling of Fe electrode in alkaline electrolyte at pH = 12.7 (50 mM KOH). a) Selected cyclic voltammograms (CVs) shown for cycles 1–20. All CVs are shown (with expanded vertical scale) in Figure S9 (Supporting Information). b-e) TEM overview images showing the structural changes before cycling (b,c) and after (d,e) 20 potential cycles. Black dotted lines show the location of the WE before and after cycling. (b,d) show the WE and (c,e) show the CE. f-h) Diffraction patterns showing newly-deposited Fe species: (f,g) BCC Fe at WE and (h) $Fe(OH)_2$ at CE after 20 CV cycles. Colors in (f-h) correspond to dotted squares regions in (d) and (e) at WE and CE respectively.

suggests that CV of Fe/Pt electrodes in alkaline solutions can enable analysis of electrochemical phenomena in Fe by correlating images and electrochemical measurements.

2.3. Interpretation of the Nanoscale Redox Behavior of the Fe Electrode at pH = 10

The peaks attributed to Fe in our typical CV scans, labelled I (Fe → Fe(II)) and II (Fe(II) → Fe(III)) in Figure 1e, translate to ≈−0.4 to −0.3 V_{SHE} and −0.1 V_{SHE} respectively based on the Pt quasi-RE calibration discussed above. The spacing between these peaks is consistent with typical CV scans for a bulk Fe electrode in alkaline electrolyte where two oxidation peaks are visible at −0.7 V_{SHE} (−0.8 $V_{Hg/HgO}$) and −0.5 V_{SHE} (−0.6 $V_{Hg/HgO}$). These are assigned to oxidation of Fe to $Fe(OH)_2$ (I) and $Fe(OH)_2$ to FeOOH (II). We note that our CV measurements are not corrected for the voltage loss caused by the electrolyte solution between WE and RE. This may account for the more positive potentials we measured in our TEM liquid cell relative to literature reported values in a standard electrochemical cell.[15]

We have mentioned the gradual but significant changes in CV with cycle number (which includes variability often present in liquid cell TEM electrochemistry data that is associated with

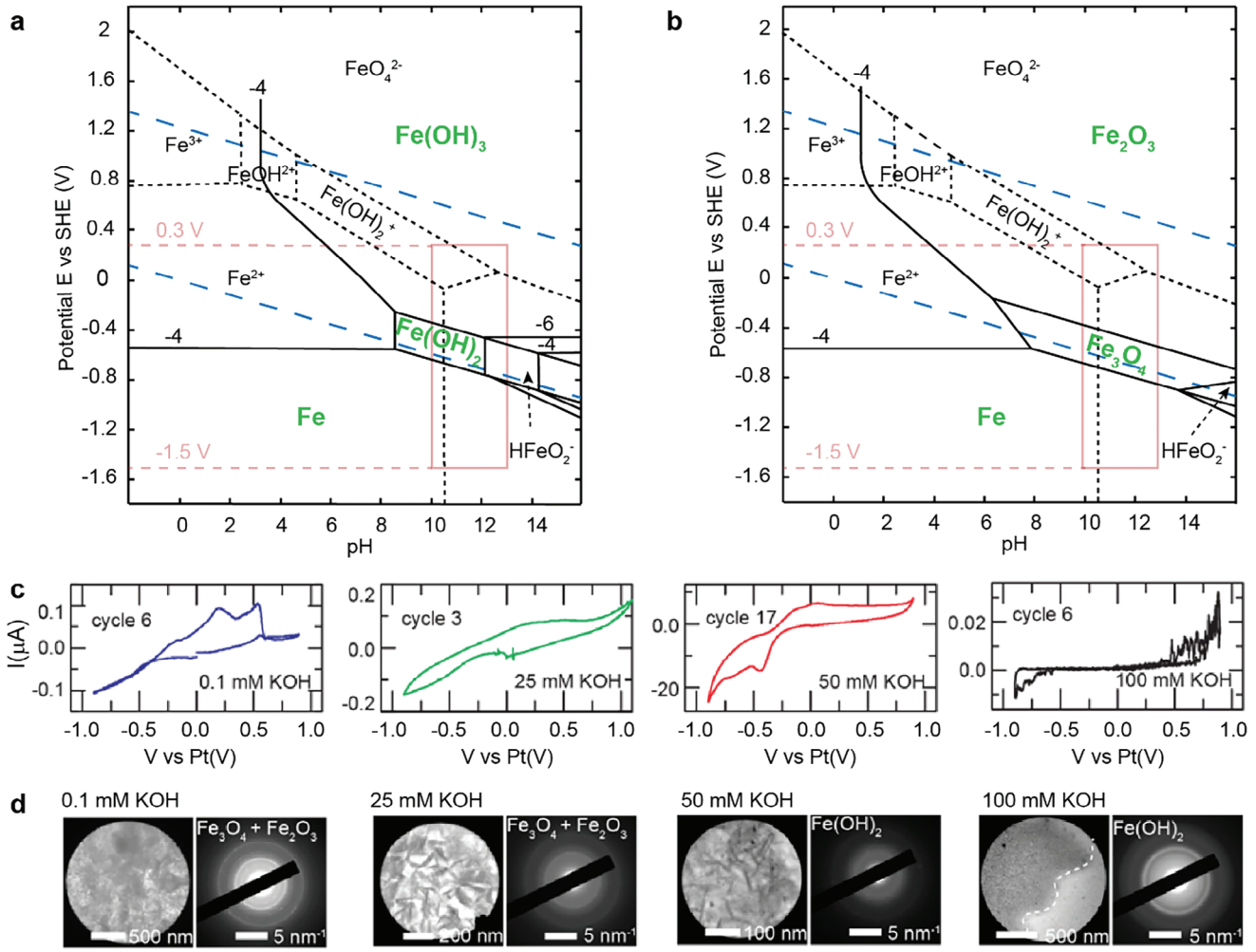

Figure 5. Effects of electrolyte pH on the formation of visible solid products during potential cycling. a,b) Fe Pourbaix diagrams at 25 °C, redrawn from[11b] and labelled with a pink box indicating the range of pH values studied and dashed lines indicating the potential cycling range. Solids in the diagram are highlighted in green, and the dotted blue lines mark the water redox reactions. Note that (a) considers only Fe, $Fe(OH)_2$ and $Fe(OH)_3$ as solid substances, while in (b) only Fe, Fe_3O_4 and Fe_2O_3 are considered. c) CVs showing redox reactions at pH 10–13 (0.1 mM to 100 mM KOH). Corresponding beaker cell CV data is shown in Figures S6 and S10 (Supporting Information). d) TEM and SAED of each experiment after potential cycling at the indicated pH values, showing the electrodeposited iron species.

phenomena such as bubble formation and depletion of electrolyte species).[17c,19] Over several experiments, cycles 1–3 typically show low but increasing redox activity, particularly in anodic oxidation. Redox activity is most prominent during cycles 4–10 (Figure S4, Supporting Information) where the two distinctive oxidation peaks I and II are observed clearly. In the subsequent cycles the activity decreases, until in cycle 20 the CV curve is almost featureless, suggesting passivation of the Fe anode. To better interpret the liquid cell TEM CV results, without the influence of electron beam-induced effects and the confinement effects imposed by the liquid cell, we conducted benchtop CV experiments at pH 10 using a three-electrode configuration in a beaker cell (Experimental Section). Unlike the liquid cell results, the beaker cell CV profiles showed no observable Fe redox peaks, indicating Fe passivation at pH 10 under bulk solution conditions. We hypothesize that the difference between the liquid cell and beaker cell results arises from a depletion of hydroxide ions within the liquid cell during CV cycling, leading to a localized decrease in pH. To support this hypothesis, we carried out additional benchtop CV measurements over the pH range 7.5–10 (Figure S6, Supporting Information). As the pH decreased, the electrochemical signals increased in the beaker cell CV data. We therefore propose that the actual pH near the Fe electrode in the liquid cell is lower than pH 10. At this lower pH, we attribute the enhanced redox activity to an increased concentration of Fe^{2+} ions, as suggested by the Pourbaix diagram. We discuss this interpretation in more detail below.

Intriguingly, the increasing redox activity in the first few cycles is also similar to the formation period for the Fe electrode that has been reported in the literature.[13,15,16,20] During the formation process of the Fe electrode (Figure 2a), the Fe first oxidizes (discharges) to iron (II) hydroxide, $Fe(OH)_2$ (**Table 1**,).[21] The conversion of Fe to $Fe(OH)_2$ is thought to occur through a multi-step dissolution-precipitation mechanism

Table 1. Discharge reactions at the Fe electrode at high pH.[11b,22a,c] In listing Equation 1, the solubility of $Fe(OH)_2$ can vary strongly with pH. According to the Pourbaix diagram, at pH ≈10.5, the main soluble species of $Fe(OH)_2$ transitions from Fe^{2+} to $HFeO_2^-$. Therefore, the formation pathway of $Fe(OH)_2$ at pH > 12 involves $HFeO_2^-$ ions and can be described by Equations (2) and (3). Note that recent studies also suggest that $HFeO_2^-$ ions can be precipitated directly to form Fe_3O_4.[22a]

$Fe + 2OH^- \leftrightarrow Fe(OH)_2 + 2e^-$	1
$Fe + 3OH^- \leftrightarrow HFeO_2^- + H_2O + 2e^-$	2
$HFeO_2^- + H_2O \leftrightarrow Fe(OH)_2 + 2OH^-$	3
$Fe(OH)_2 + OH^- \leftrightarrow FeOOH + H_2O + e^-$	4
$3Fe(OH)_2 + 2OH^- \leftrightarrow Fe_3O^4 \cdot 4H_2O + e^-$	5
$2Fe_3O_4 + 2OH^- \leftrightarrow 3Fe_2O_3 + H_2O + 2e^-$	6

(Equations 2 and 3): adsorption of hydroxide ions onto the Fe surface, formation of soluble ferrite ion ($HFeO_2^-$) (Equation 2), and precipitation of ferrite ions onto the Fe surface as solid $Fe(OH)_2$ due to their low solubility (Equation 3).[22] On the reverse part of the cycle the $Fe(OH)_2$ undergoes reduction (charging) to Fe and is deposited on different surface sites on the electrode, thereby increasing the roughness and EASA of the electrode. However, when the $Fe(OH)_2$ is not fully reduced back to Fe, the residual surface hydroxide will decrease the EASA. The end of the formation process is reached when the growth of EASA from Fe deposition during charging becomes equal to the EASA lost to residual hydroxide in discharging.[7d,11a,13] This hydroxide layer prevents complete discharge and limits the utilization of the Fe electrode. A greater discharge capacity can be achieved when the hydroxide is further discharged to ferric oxyhydroxide (Equation 4), magnetite (Equation 5) or hematite (Equation 6)[7d,11a] but the deeper discharge (Figure 2b) creates Fe (III) products that have traditionally been more difficult to cycle reversibly and eventually suppress the redox activity, which also significantly limits the use of the Fe electrode.[21,23]

Microstructural changes are expected to accompany this cycling. At the periphery of our Fe thin film electrode, we observe a substantial build-up of distinctive needle-like features after the 20-cycle process (Figure 1g,h). The identity of the material is not obvious from the contrast since this type of TEM image (recorded under bright field conditions) is mainly sensitive to the atomic number and the various oxides are not readily distinguishable from image contrast alone. We therefore obtainSAED data to identify the Fe oxide species after cycling. We find that these deposits comprise three identifiable phases. BCC Fe is present, similar to initial Fe (Figure 2c), formed presumably by reduction of oxidized products (Figure 2d). In addition, Fe_3O_4 and Fe_2O_3 can be detected (Figures 1i,j and 2e–g). However, we do not see distinguishable diffraction that is characteristic of $Fe(OH)_2$ or FeOOH. We thus observe the deep-discharge products[24] that are known to be poorly reversible, particularly in the absence of sulfide ions.[12a,25]

We interpret the microstructural and electrochemical results of the cycling at pH = 10 through the Pourbaix diagram of Fe, shown in Figure 5a,b.[11a] The Pourbaix diagram suggests that around pH 10, the primary soluble species of $Fe(OH)_2$ shifts from $HFeO_2^-$ to Fe^{2+}, with Fe^{2+} concentration higher at lower pH. This leads us to propose that the increase in observed redox activity during CV cycling is linked to local decrease in pH and increase in Fe^{2+} concentration. The absence of anodic peaks in the initial liquid cell CV cycles and our beaker cell CV data (Figure S6, Supporting Information) support this hypothesis. We also note that pH = 10 is still in the $Fe(OH)_2$ stability regime where formation of a passivation product is expected. This is consistent with the observation of material deposited at the WE. It is unclear, however, whether the passivating oxides are formed by over-oxidation of Fe beyond $Fe(OH)_2$, or by deposition from ions released into solution. Considering the evolution of the electrochemical signals during cycling and the potential range used, a reasonable interpretation is that passivation of the Fe electrode has led to the decreased electrochemical activity by cycle 20. The appearance of oxides, rather than hydroxides, suggests that the Fe electrode is deeply oxidized beyond the stability range of the hydroxide products. The absence of an obvious reduction peak in the CV data further suggests that any hydroxide species have been oxidized to form the oxides observed (Figure 2b).

It is also notable from the images that the Pt CE also appears to be passivated with oxide after cycling. Given the voltage swings, this electrode also reaches both highly reducing and highly oxidizing potentials. The formation of needle-like Fe species at the CE suggests that some transport has occurred over a distance, indicating the presence of soluble species even within the iron hydroxide and iron oxide stability regime of the Pourbaix diagram. Our speculation is that here Fe^{2+} and $Fe(OH)_2^+$ ions may be responsible for the visible electrodeposition at the Pt CE. This is because at pH 10, $Fe(OH)_2$ can theoretically dissolve to form ≈10^{-7} M Fe^{2+} ions and, as predicted by the Pourbaix diagram (Figure 5a,b), $Fe(OH)_2^+$ ions become a thermodynamically stable soluble phase at pH 10 with potential > ≈0.2 V_{SHE}.[11b] Thus, our experimental results suggest some solubility of Fe species, enabling Fe ion diffusion and re-deposition elsewhere in the electrochemical cell. In the battery this could contribute to the overall roughening process and increase the EASA of the electrode during the formation process, eventually leading to a higher discharge capacity at the end of the formation process.

2.4. Real-Time Imaging of the Fe Electrode During Potential Cycling at pH = 10

To confirm that the oxidized Fe species we observe post-cycling in liquid cell experiments do in fact arise from electrochemical reactions at the Fe, and to measure the kinetics of their formation, we image the electrodes continuously in the TEM during cycling under the conditions used in Figure 1. Continuous imaging enables reaction kinetics to be probed (Figure 3) but opens the possibility of electron beam influence on the reaction. We find that electron beam effects do occur in these experiments. Most notably, we observe rapid dissolution of Fe thin film during the reduction part of the third CV cycle (Figure 3a,b, blue curve). We discuss this below in terms of the expected effect of irradiation in increasing the concentration of H^+ ions in the irradiated electrolyte. However, upon oxidation (Figure 3b, black curve) the dissolution stops, and a thin surface layer formed at t = 89.6–106.4 s (Figure 3b, red arrows). The potential and integrated current response (Figure 3c–e) shows that an irreversible charge passes during the cycle. This residual charge could be due

to side reactions such as gas formation from hydrogen evolution reaction (HER), which is a well-known parasitic side reaction for Fe electrodes.[20]

We further characterized the microstructure post-cycling (Figure S7, Supporting Information) and we suggest this thin layer is oxidized Fe, as it resembles the needle-like structure that we observed *ex situ* (Figure 3f). Overall, the in situ measurements in Figure 3 demonstrate two features of cycling: the newly electrodeposited needle-like Fe species is Fe_3O_4, and a blocking layer forming across WE, RE and CE (Figure 3g). The absence of Fe_2O_3 suggests that the reaction in Equation 6 does not occur during the initial CV cycles. The formation of over-discharged Fe (III) products is primarily driven by multiple charging-discharging cycles, associated with the discharge capacity of the Fe electrode. We have confirmed this observation for Fe electrode potential cycling at pH = 10 and show further examples in Figure S8 (Supporting Information). These two observations are consistent with the results after cycling in the experiments described previously.

2.5. Comparison with Potential Cycling at Higher pH

To explore the predicted changes in Fe electrochemistry with pH and approach the higher operating pH values of the alkaline iron battery, we also examined the behavior of the Fe electrode in liquid cells with higher KOH concentrations. In particular, we focused on a transition pH range of 12.7–13, where the Pourbaix diagram suggests that the Fe electrode enters the corrosion regime. Results obtained at pH = 12.7 (50 mM KOH) are shown in Figure 4. The activity is low during the first several cycles, which can be attributed to the presence of the native iron oxide layer,[15] as only the reduction reaction peak can be observed initially (Figure S9, Supporting Information). Subsequently, due to the gradual removal of the surface oxide layer, the activity increases to a level that is higher than at pH = 10, as seen from the scale of the graphs in the CV traces (Figure 4a; Figure S8, Supporting Information). This higher current flow persists over the complete measurement, 20 cycles. In the TEM images, some dissolution of Fe is evident as the edge of the electrode recedes (Figure 4d) and some deposition is also present near and on the electrode; from diffraction this deposit appears to be composed of BCC Fe (Figure 4f,g). Near the Pt CE, only minor deposits (Figure 4h) that include $Fe(OH)_2$ are detectable. The substantial amounts of deposition observed at lower pH are absent in this experiment. Importantly, even at 20 cycles the CVs in Figure 4a show both anodic and cathodic peaks, indicating that at this high pH the reaction likely proceeds reversibly. Furthermore, we find that the liquid cell CV profiles at pH 12.7 align closely with those in the beaker cells (Figure S10, Supporting Information).

The increased activity is consistent with our expectation that electrochemical activity should increase at higher pH: alkaline Fe batteries show relatively low capacity when $[OH^-]$ is below 1 M.[7a,14a] The changes in redox activity and microstructural changes at pH = 12.7 can be considered in the context of the amount of soluble Fe species produced, their increased solubility at higher pH,[26] as well as changes in the conductivity of the electrolyte. These factors may result in deposition elsewhere in the cell (Figure 2b). The solubility of $Fe(OH)_2$ is minimized at pH = 10.5 but by pH = 12.7 the solubility has increased by two orders of magnitude and the solubility product of $Fe(OH)_2$, i.e., $HFeO_2^-$ ions, has increased dramatically.[11b] This is also consistent with literature reports that the conductivity for KOH aqueous solution increases linearly in the low concentration range.[26] Thus, the increase in solubility above its minimum at pH = 10.5 may underpin the changes in electrochemical and microstructural behavior of the Fe electrode, a factor that is not generally emphasized in the literature.[11b,27]

We summarize this series of potential cycling experiments in Figure 5. The first three data sets shown are those in Figures 1 and 4 and another at an intermediate pH. Over this pH range we consistently observe an initially low redox activity, described earlier in terms of a formation time, that increases after the first several cycles to a level of activity that is higher at pH = 12.7 than pH = 10. Fe dissolution is observed in all experiments, and deposited material is visible on the WE and RE, more so at lower pH. At longer times, the lower pH experiments (pH = 10) show an eventual decrease in redox activity that may arise from the formation of a passivating oxide layer visible after multiple cycles. In contrast, at higher pH (pH = 12.7) the higher activity remains for over 20 cycles with extensive deposits not visible, and the CVs (Figure 4a) show a reduction peak of iron indicating that at this high pH the reaction proceeds more reversibly.

As we move to pH = 13 this pattern changes (Figure 5c,d). In the liquid cell the measured electrochemical activity is lower (note the change in scale) and the structural features present in the lower pH experiments are not visible. In the beaker cell the Fe electrode remains active with both oxidation and reduction peaks of Fe present (Figure S10, Supporting Information). This difference can be attributed to the formation of $HFeO_2^-$ and its solubility changes during CV cycling. pH = 13 lies in the corrosion regime in the Pourbaix diagram: $HFeO_2^-$ ions, which could be formed from the reduction of the native iron oxide layer or the dissolution from the pristine Fe (Equation 2) with the evolution of hydrogen, dictate the iron redox kinetics.[11b] Here we speculate that $HFeO_2^-$ ions can rapidly exceed their solubility at pH = 13 ($\approx 5 \times 10^{-6}$ M) within the confined liquid cell environment, and more importantly, the consumption of hydroxide ions during the anodic sweep, which lowers their concentration near the WE, can decrease the solubility of $HFeO_2^-$. The increase in concentration and decrease in solubility of ferrite ions can facilitate the formation of $Fe(OH)_2$ layer on the electrode surface within the liquid cell (detected in diffraction in Figure 5c), thus blocking the redox reaction.

2.6. Beam-Induced Chemical Changes

One of the most important experimental issues in liquid cell TEM is the influence of the electron beam on solution chemistry. We can calculate the ion concentrations expected during irradiation with electrons. Such calculations have been performed for neat water, although not for most solutions of interest, as the presence of each ion species affects the equilibrium concentration of the other species through coupled reactions. It has been shown[28] that the steady-state concentration of H^+ ions in aqueous electrolytes increases with electron dose rate, to the extent that an electrolyte initially with $[H^+] = 10^{-14}$ M (i.e., pH = 14) can change to $[H^+] = 10^{-8}$ M at high dose rate.[17c] This does not directly

imply that the solution is at pH = 8 because the irradiated volume is not in equilibrium and [OH^-] is also affected by irradiation.[29] As an example, and neglecting any other ions present, irradiation of a solution of pH = 10 at an electron flux of 45 e^- $Å^{-2}$·s or 2.0 x 10^8 Gy s^{-1} results in an increase of [H^+] from 10^{-10} M to 10^{-6} M while leaving [OH^-] almost unchanged at 10^{-4} M.

Such beam-induced changes in solution chemistry are not directly visible in the experiments but can affect reactions with materials in contact with the solution. We have observed dissolution of the Fe film in the pH = 10 electrolyte upon irradiation at an electron flux of 45 e^- $Å^-2$ s^{-1}, as shown in Figure S11 (Supporting Information). As the beam is moved to a new area, pitting starts immediately with dissolution following within a few minutes. Under the beam, we expect [H^+] = 10^{-6} M. According to the Fe Pourbaix diagram,[11b] a decrease in the pH to 6 would place the system in a corrosion regime where metallic Fe dissolves to Fe^{2+} in solution. At higher dose rate (100 e^- $Å^-2$ s^{-1} or 4.5×10^8 Gy s^{-1}), again without applied bias, we also observe formation of FCC Fe islands (Figure S12, Supporting Information). This is also consistent with dissolution of Fe via increased [H^+], followed by reduction and redeposition of the Fe ions via reaction with hydrated electrons, another species created by radiolysis. Corrosion followed by redeposition has been observed in other liquid cell experiments[30] while FCC Fe island formation has also been reported[31] directly from iron sulphate solution. By maintaining lower dose rate we avoid visible formation of FCC Fe islands.

These two observations lead us to conclude that Fe dissolution, presumably mediated by beam-induced increase in [H^+], takes place under in situ observation. The dose rate determines the radiolysis species and hence the expected reaction pathway and rate. The applied voltage provides an additional parameter to tune reactions in the liquid cell. In particular, dissolution of the Fe electrode is expected at pH = 8 when unbiased, but when biased, Fe should become stable at −0.6 V_{SHE} according to the Pourbaix diagram. Thus we can take advantage of beam effects to design unique experiments, using radiolytic changes in local solution chemistry to explore the Pourbaix diagram. It is not possible to eliminate beam effects, but lowering the dose rate[30,32] and using scavengers such as graphene[33] or isopropanol[34] in liquid cell experiments offer strategies to mitigate beam effects. Minimizing beam exposure of the Fe during electrochemical measurements as well as comparison of in situ and *ex situ* data are crucial to increase our confidence in interpretation of electrochemical data.

3. Discussion

In our CV cycling experiments within the liquid cell environment, we observe distinctive electrochemical behavior at pH = 10 compared to other pH values. Initially, the Fe electrode shows low redox activity, which increases with CV cycling but later decreases again. Microscopy indicates that BCC Fe forms upon reduction of oxidized products in both in situ and identical-location studies. At strongly oxidizing potentials, we observe the passivation of the Fe electrode by Fe_3O_4 and Fe_2O_3, which accumulate to form a blocking layer across the electrodes in later cycles, resulting in featureless CV profiles. This is consistent with previous literature results showing that reversibility is strongly dependent on the extent of oxidation, and, more importantly, the charging conditions applied.[13,35] Interestingly, our observation of the deposition of deeply oxidized products (Fe_3O_4 and Fe_2O_3) on the CE, where there was no starting Fe, suggests that a solution-precipitation mechanism is operative. We speculate that this deposition is a result of the buildup of a concentration gradient of certain soluble species, which are assumed to be $Fe(OH)_2^+$ or Fe^{2+} based on the Pourbaix diagram for the potential range applied. Comparison with benchtop experiments suggests that depletion of the local hydroxide concentration in the liquid cell during the anodic sweep may shift the system toward the soluble Fe^{2+} region, slightly increasing the solubility of $Fe(OH)_2$, resulting in a higher concentration of Fe^{2+} ions.[11b] This mechanism also explains the increase in redox activity observed in the liquid cell during CV cycling.

Our results also show that as the solution pH shifts toward higher values, notably pH = 13, iron redox reactions can be inhibited by the formation of an iron hydroxide layer on the electrode. This passivating layer of iron hydroxide is easy to form, presumably due to a decrease in the solubility of ferrite ions resulting from the depletion of hydroxide ions. Addressing the issue of low Fe redox activity may require suppression of the HER and enhanced solubility of the ferrite ions. This could be achieved through additives such as Bi_2S_3 and Na_2S, or by operating at pH above 13, which is more representative of typical battery operating conditions.[25] Both of these strategies would benefit from future in situ investigation, which may require modifications to current designs of liquid cell TEM holders and chips to ensure their viability in even more highly alkaline environments.

It is important to acknowledge that the liquid cell is not a precise model for an actual electrochemical device due to the small electrolyte volume and the effects of the beam. Our comparative experiments in a beaker allowed us to assess these limitations. At pH 12.4 and 12.7 the liquid cell and beaker cell results were similar, while differences arose at pH 10 and pH 13. We explained these differences by again using the Fe Pourbaix diagram, considering the depletion of hydroxide ions and changes in the solubility of soluble Fe species, both associated with the limited electrolyte volume. Thus it is possible to probe the effects of insufficient electrolyte volume, i.e., depletion effects, on the electrochemical behavior of the system, especially at low KOH concentrations.

Overall, our liquid cell observations can largely be understood using the Pourbaix diagram, which provides insight into iron hydroxide/oxide formation, the presence of some soluble Fe species, and the extent of local pH changes during CV cycling. Importantly, we conclude that it is essential to consider kinetic effects as part of the overall process, including the solubility and diffusion of Fe species, the kinetics of discharge product formation and accumulation, and electrolyte depletion. These processes, which are strongly dependent on the local pH and applied potential, have a significant impact on the transport of materials within the working cell.

4. Conclusion and Outlook

In this work, we have described the electrochemical response and microstructural evolution of Fe electrodes in alkaline media as a function of pH during CV cycling by combining identical

location imaging and diffraction, in situ imaging, and benchtop electrochemical measurements. Our findings reveal a strong dependence of electrochemical reactivity of Fe electrodes on electrolyte pH, with a significant difference between passivation behavior and the formation of soluble species as we move across the pH range from 10 to 13. Through comparative analysis of data obtained from liquid cell and benchtop beaker cell experiments, we stress the importance of kinetic factors in the overall electrochemical process, particularly the solubility and diffusion of Fe species, electrolyte depletion and the formation and accumulation of discharge product. By combining these kinetic considerations with equilibrium thermodynamic insights from the Pourbaix diagram, we provide a detailed understanding of the behavior of Fe anodes in the confined liquid cell environment. For battery materials in complex aqueous media, we propose that identical-location and in situ imaging offer a feasible and reliable approach to capture unique information on discharge and charge processes. We anticipate that our combined approach in this study can establish a foundation for optimizing electrochemical liquid cell TEM experiments for other electrochemical systems, particularly those involving complex, high-pH electrolytes with additives that are critically relevant to real-world applications.

In future, we anticipate that developments in liquid cell technique will enable more quantitative measurement of liquid phase diffusion and chemistry. This will be achieved by using electron beam effects to analyze local chemistry, incorporating an in-holder true reference electrode to calibrate the RE potential,[36] and optimizing liquid cell and electrode designs to control liquid volume and diffusion pathways,[18b,37] thereby mitigating confinement effects. Integrating electrodes with heating circuits in the liquid cell will further enable studies on temperature-dependent electrochemical reactions,[17b,38] thus expanding the scope of the liquid cell technique for real-world applications. Based on such developments, we are particularly excited by the possibilities of observing formation of passivation layers, failure modes, influence of metal microstructure, and the effect of electrolyte additives in metal-air batteries, which will guide improvements in the performance of this important class of energy storage solutions.

5. Experimental Section

Sample Preparation: Potassium hydroxide and potassium chloride were used as-received without further purification. All aqueous solutions were prepared using deionized water.

Experimental Procedures: For in situ and identical-location electrochemical cell experiments, each electrochemical cell consisted of a 100 nm spacer chip with 30 nm thick SiN_x membrane window (Hummingbird Scientific, Lacey, WA, USA) and a modified electrochemical chip with 50 nm thick SiN_x membrane window and Pt electrodes (Hummingbird Scientific, Lacey, WA, USA), on which Fe was deposited directly. Before assembling the electrochemical cell, the spacer chip was cleaned with an oxygen plasma for 1 min to render its surface hydrophilic. Each electrochemical cell was assembled and loaded into an analytical flow holder (Hummingbird Scientific, Lacey, WA, USA). The Pt pseudo-reference electrode calibration was carried out using a Gen V bulk liquid electrochemistry TEM holder[36] (Hummingbird Scientific, Lacey, WA, USA) against a bulk reference electrode Ag/AgCl that were placed near to the liquid cell chip in a tiny disk-like geometry, 0.55 mm diameter and 0.2 mm height, saturated with 0.1 M KCl. After checking and confirming no leaks in the flow cell, the holder was inserted into a JEOL 2011 TEM operated at 200 kV for in situ and identical-location studies, where the incident electron flux ranged from 6 to 30 e^{-} Å^{-2} s^{-1}. Image series were acquired at 10–30 frames per second using an AMT camera (AMT Imaging, Woburn, MA, USA). The alkaline solution (0.1 mM, 25 mM, 50 mM and 100 mM KOH) was introduced into the liquid cell via a flow tube (diameter of 200 µm and length of 50 cm) connected to a syringe pump, using a flow rate of 3–5 µL min^{-1}. It took a few minutes for the solution to reach the window area of the electrochemical cell. On the videos, $t = 0$ s corresponds to application of voltage to the electrodes. The electrochemical measurements were made using a Gamry Reference 600+ potentiostat (Gamry Instruments, Pennsylvania, USA). Post-deposition high resolution TEM (HAADF-STEM) imaging and diffraction analysis were performed with a JEOL 2010F operated at 200 kV. In benchtop experiments, a three-electrode setup was utilized, including an iron electrode (10 mm × 10 mm × 0.25 mm, 99.5%, GoodFellow, England) as the working electrode (WE), a Hg/HgO electrode (BASi, USA) as the reference electrode (RE), and a Pt electrode (StonyLab, USA) as the counter electrode (CE). KOH (Sigma–Aldrich, USA) was used to prepare electrolytes and the desired pH (7.5, 8, and 10) was ensured by a pH meter (Apera Instruments, pH700, USA). CV measurements were carried out at room temperature using a multichannel potentiostat (BioLogic VMP3, France) with a scan rate of 20 mV s^{-1}. The resulting CV data were processed and visualized in MATLAB (MathWorks, USA).

Supporting Information

Supporting Information is available from the Wiley Online Library or from the author.

Acknowledgements

The authors acknowledge funding from the U.S. DOE Advanced Research Projects Agency-Energy under award DE-AR0000995.

Conflict of Interest

The authors declare no conflict of interest.

Data Availability Statement

The data that support the findings of this study are available from the corresponding author upon reasonable request.

Keywords

electrochemical reactivity, Fe batteries, liquid cell, stability, TEM

Received: May 3, 2024
Revised: November 5, 2024
Published online: December 2, 2024

[1] BP. *Statistical Review of World Energy 2022*, 71st ed.; BP, London, UK, **2022**, https://www.bp.com/en/global/corporate/energy-economics/statistical-review-of-world-energy.html.
[2] M. R. Shaner, S. J. Davis, N. S. Lewis, K. Caldeira, *Energy Environ. Sci.* **2018**, *11*, 914.
[3] a) M. S. Ziegler, J. M. Mueller, G. D. Pereira, J. Song, M. Ferrara, Y.-M. Chiang, J. E. Trancik, *Joule* **2019**, *3*, 2134; b) P. Albertus, J. S. Manser, S. Litzelman, *Joule* **2020**, *4*, 21.

[4] a) R. E. Ciez, J. Whitacre, *J. Power Sources* **2016**, *320*, 310; b) W. A. Braff, J. M. Mueller, J. E. Trancik, *Nat. Clim. Change* **2016**, *6*, 964; c) S. J. Davis, N. S. Lewis, M. Shaner, S. Aggarwal, D. Arent, I. L. Azevedo, S. M. Benson, T. Bradley, J. Brouwer, Y.-M. Chiang, *Science* **2018**, *360*, eaas9793.
[5] H.-F. Wang, Q. Xu, *Matter* **2019**, *1*, 565.
[6] T. A. Edison, US Patent 678722, **1901**.
[7] a) S. Sripad, A. Bills, V. Viswanathan, *ECSarXiv* **2021**, https://doi.org/10.1149/osf.io/fx4p9; b) R. McKerracher, C. Ponce de Leon, R. Wills, A. A. Shah, F. C. Walsh, *ChemPlusChem* **2015**, *80*, 323; c) W. H. Woodford, S. Burger, M. Ferrara, Y.-M. Chiang, *One Earth* **2022**, *5*, 212; d) S. Narayanan, G. S. Prakash, A. Manohar, B. Yang, S. Malkhandi, A. Kindler, *Solid State Ionics* **2012**, *216*, 105.
[8] a) S. Liu, C. Li, M. J. Zachman, Y. Zeng, H. Yu, B. Li, M. Wang, J. Braaten, J. Liu, H. M. Meyer III, *Nat. Energy* **2022**, *7*, 652; b) A. Mehmood, M. Gong, F. Jaouen, A. Roy, A. Zitolo, A. Khan, M.-T. Sougrati, M. Primbs, A. M. Bonastre, D. Fongalland, *Nat. Catal.* **2022**, *5*, 311; c) H. Zhang, S. Hwang, M. Wang, Z. Feng, S. Karakalos, L. Luo, Z. Qiao, X. Xie, C. Wang, D. Su, *J. Am. Chem. Soc.* **2017**, *139*, 14143; d) M. Lefèvre, E. Proietti, F. Jaouen, J.-P. Dodelet, *Science* **2009**, *324*, 71.
[9] K. Gong, X. Ma, K. M. Conforti, K. J. Kuttler, J. B. Grunewald, K. L. Yeager, M. Z. Bazant, S. Gu, Y. Yan, *Energy Environ. Sci.* **2015**, *8*, 2941.
[10] Z. Li, M. S. Pan, L. Su, P.-C. Tsai, A. F. Badel, J. M. Valle, S. L. Eiler, K. Xiang, F. R. Brushett, Y.-M. Chiang, *Joule* **2017**, *1*, 306.
[11] a) H. Weinrich, Y. E. Durmus, H. Tempel, H. Kungl, R.-A. Eichel, *Materials* **2019**, *12*, 2134; b) M. Pourbaix, *Atlas of electrochemical equilibria in aqueous solutions*, National Association of Corrosion Engineers, Houston, Texas **1974**.
[12] a) A. K. Manohar, C. Yang, S. Narayanan, *J. Electrochem. Soc.* **2015**, *162*, A1864; b) J. O. G. Posada, P. J. Hall, *J. Power Sources* **2014**, *268*, 810.
[13] H. Weinrich, M. Gehring, H. Tempel, H. Kungl, R.-A. Eichel, *J. Appl. Electrochem.* **2018**, *48*, 451.
[14] a) L. Öjefors, L. Carlsson, *J. Power Sources* **1978**, *2*, 287; b) K. Vijayamohanan, A. Shukla, S. Sathyanarayana, *J. Power Sources* **1990**, *32*, 329.
[15] H. Weinrich, J. Come, H. Tempel, H. Kungl, R.-A. Eichel, N. Balke, *Nano Energy* **2017**, *41*, 706.
[16] A. K. Manohar, C. Yang, S. Malkhandi, B. Yang, G. S. Prakash, S. Narayanan, *J. Electrochem. Soc.* **2012**, *159*, A2148.
[17] a) S. F. Tan, K. Reidy, J. Klein, A. Pinkowitz, B. Wang, F. M. Ross, *Chem. Sci.* **2021**, *12*, 5259; b) S. F. Tan, K. Reidy, S. Lee, J. Klein, N. M. Schneider, H. Y. Lee, F. M. Ross, *Adv. Funct. Mater.* **2021**, *31*, 2104628; c) F. M. Ross, *Science* **2015**, *350*, aaa9886.
[18] a) W. Alnoush, R. Black, D. Higgins, *Chem. Catal.* **2021**, *1*, 997; b) T. H. Shen, R. Girod, J. Vavra, V. Tileli, *J. Electrochem. Soc.* **2023**, *170*, 056502.
[19] a) R. Serra-Maia, P. Kumar, A. C. Meng, A. C. Foucher, Y. Kang, K. Karki, D. Jariwala, E. A. Stach, *ACS Nano* **2021**, *15*, 10228; b) N. Hodnik, G. Dehm, K. J. Mayrhofer, *Acc. Chem. Res.* **2016**, *49*, 2015. c) Y. Pan, X. Li, D. Su, *Curr. Opin. Electrochem.* **2022**, *33*, 100936.
[20] H. Weinrich, J. Pleie, B. Schmid, H. Tempel, H. Kungl, R. A. Eichel, *Batteries Supercaps* **2022**, *5*, 202100415.
[21] B. Andersson, L. Öjefors, *J. Electrochem. Soc.* **1976**, *123*, 824.
[22] a) B. M. Weninger, M. A. Thijs, J. A. Nijman, L. van Eijck, F. M. Mulder, *J. Phys. Chem. C* **2021**, *125*, 16391; b) J. Černý, K. Micka, *J. Power Sources* **1989**, *25*, 111; c) D. Dražić, C. S. Hao, *Electrochim. Acta* **1982**, *27*, 1409; d) R. Armstrong, I. Baurhoo, *J. Electroanal. Chem. Interfacial Electrochem.* **1972**, *34*, 41.
[23] K. Micka, Z. Zábranský, *J. Power Sources* **1987**, *19*, 315.
[24] J. Jiang, J. Liu, *Interdisciplinary Mater.* **2022**, *1*, 116.
[25] Z. He, F. Xiong, S. Tan, X. Yao, C. Zhang, Q. An, *Mater. Today Adv.* **2021**, *11*, 100156.
[26] R. J. Gilliam, J. Graydon, D. Kirk, S. Thorpe, *Int. J. Hydrogen Energy* **2007**, *32*, 359.
[27] B. Morgan, O. Lahav, *Chemosphere* **2007**, *68*, 2080.
[28] N. M. Schneider, M. M. Norton, B. J. Mendel, J. M. Grogan, F. M. Ross, H. H. Bau, *J. Phys. Chem. C* **2014**, *118*, 22373.
[29] B. Fritsch, A. Körner, T. Couasnon, R. Blukis, M. Taherkhani, L. G. Benning, M. P. Jank, E. Spiecker, A. Hutzler, *J. Phys. Chem. Lett.* **2023**, *14*, 4644.
[30] J. H. Park, D. A. Steingart, S. Kodambaka, F. M. Ross, *Sci. Adv.* **2017**, *3*, e1700234.
[31] U. Wolff, B. Ambrozic, K. Z. Rozman, K. Leistner, K. Nielsch, S. Sturm, *Microsc. Microanal.* **2018**, *24*, 310.
[32] a) J. H. Park, N. M. Schneider, J. M. Grogan, M. C. Reuter, H. H. Bau, S. Kodambaka, F. M. Ross, *Nano Lett.* **2015**, *15*, 5314; b) T. Woehl, P. Abellan, *J. Microscopy* **2017**, *265*, 135; c) J. Hermannsdörfer, N. De Jonge, A. Verch, *Chem. Commun.* **2015**, *51*, 16393; d) H. Wu, T. Li, S. P. Maddala, Z. J. Khalil, R. R. M. Joosten, B. Mezari, E. J. M. Hensen, G. de With, H. Friedrich, J. A. van Bokhoven, J. P. Patterson, *ACS Nano* **2021**, *15*, 10296.
[33] a) H. Cho, M. R. Jones, S. C. Nguyen, M. R. Hauwiller, A. Zettl, A. P. Alivisatos, *Nano Lett.* **2017**, *17*, 414; b) Y. Qiu, Z. Wang, A. C. Owens, I. Kulaots, Y. Chen, A. B. Kane, R. H. Hurt, *Nanoscale* **2014**, *6*, 11744.
[34] J. Korpanty, L. R. Parent, N. C. Gianneschi, *Nano Lett.* **2021**, *21*, 1141.
[35] a) Y. Geronov, T. Tomov, S. Georgiev, *J. Appl. Electrochem.* **1975**, *5*, 351; b) H. G. Silver, E. Lekas, *J. Electrochem. Soc.* **1970**, *117*, 5; c) A. J. Salkind, C. Venuto, S. U. Falk, *J. Electrochem. Soc.* **1964**, *111*, 493.
[36] K. Karki, R. Serra-Maia, E. Stach, D. H. Alsem, N. Salmon, *Microsc. Microanal.* **2020**, *26*, 1458.
[37] H. Wu, H. Su, R. R. Joosten, A. D. Keizer, L. S. van Hazendonk, M. J. Wirix, J. P. Patterson, J. Laven, G. de With, H. Friedrich, *Small Methods* **2021**, *5*, 2001287.
[38] S. Lee, N. M. Schneider, S. F. Tan, F. M. Ross, *ACS Nano* **2023**, *17*, 5609.